High-resolution tomography of positron emitters with clustered pinhole SPECT

2010 Phys. Med. Biol. 55 1265

(http://iopscience.iop.org/0031-9155/55/5/001)

IOP PUBLISHING PHYSICS IN MEDICINE AND BIOLOGY

Phys. Med. Biol. **55** (2010) 1265–1277 doi:10.1088/0031-9155/55/5/001

High-resolution tomography of positron emitters with clustered pinhole SPECT

Marlies C Goorden[1,2] **and Freek J Beekman**[1,2,3]

[1] Section of Radiation Detection and Medical Imaging, Applied Sciences, Delft University of Technology, Mekelweg 15, 2629 JB Delft, The Netherlands
[2] Image Sciences Institute and Rudolf Magnus Institute, University Medical Center Utrecht, Heidelberglaan 100, 3584 CX Utrecht, The Netherlands
[3] Molecular Imaging Laboratories, Universiteitsweg 100, 3584 CG Utrecht, The Netherlands

E-mail: m.c.goorden@tudelft.nl

Received 15 October 2009, in final form 29 December 2009
Published 4 February 2010
Online at stacks.iop.org/PMB/55/1265

Abstract

State-of-the-art small-animal single photon emission computed tomography (SPECT) enables sub-half-mm resolution imaging of radio-labelled molecules. Due to severe photon penetration through pinhole edges, current multi-pinhole SPECT is not suitable for high-resolution imaging of photons with high energies, such as the annihilation photons emitted by positron emitting tracers (511 keV). To deal with this edge penetration, we introduce here clustered multi-pinhole SPECT (CMP): each pinhole in a cluster has a narrow opening angle to reduce photon penetration. Using simulations, CMP is compared with (i) a collimator with traditional pinholes that is currently used for sub-half-mm imaging of SPECT isotopes (U-SPECT-II), and (ii), like (i) but with collimator thickness adapted to image high-energy photons (traditional multi-pinhole SPECT, TMP). At 511 keV, U-SPECT-II is able to resolve the 0.9 mm rods of an iteratively reconstructed Jaszczak-like capillary hot rod phantom, and while TMP only leads to small improvements, CMP can resolve rods as small as 0.7 mm. Using a digital tumour phantom, we show that CMP resolves many details not assessable with standard USPECT-II and TMP collimators. Furthermore, CMP makes it possible to visualize uptake of positron emitting tracers in sub-compartments of a digital mouse striatal brain phantom. This may open up unique possibilities for analysing processes such as those underlying the function of neurotransmitter systems. Additional potential of CMP may include (i) the imaging of other high-energy single-photon emitters (e.g. I-131) and (ii) localized imaging of positron emitting tracers simultaneously with single photon emitters, with an even better resolution than coincidence PET.

1. Introduction

Molecular imaging of small animals with SPECT is rapidly gaining popularity. Small-animal SPECT is a key tool in the development of tracers (radio-labelled), pharmaceuticals and in the study of animal models of human disease (Andringa *et al* 2005, Zhou *et al* 2005, Wild *et al* 2006, Vastenhouw *et al* 2007b, Blanckaert *et al* 2009, Davis *et al* 2009, Deroose *et al* 2009, Nikolaus *et al* 2009, van der Have *et al* 2009). Image resolution of SPECT systems dedicated to imaging small animals has improved dramatically over the past few decades (Strand *et al* 1994, Jaszczak *et al* 1994, Ishizu *et al* 1995, Liu *et al* 2002, McElroy *et al* 2002, Schramm *et al* 2003, Furenlid *et al* 2004, Walrand *et al* 2005, Metzler *et al* 2005, Funk *et al* 2006, Hesterman *et al* 2007). Recently developed SPECT devices with stationary detectors and focusing multi-pinhole collimators (MP-SPECT) provide sub-half-mm image resolution (Beekman *et al* 2005, Beekman and van der Have 2007a, Vastenhouw *et al* 2007b, van der Have *et al* 2009), which allows monitoring of tracer uptake in much smaller structures than is possible with state-of-the-art small-animal PET (approx. 1 mm resolution). The high resolution of pinhole SPECT compared to PET can be explained by the higher information content per detected gamma photon with pinhole SPECT, despite the lower sensitivity (fraction of emitted photons detected) of SPECT. This naturally raises the question of whether cases exist in which positron emitting tracers can be imaged at a high resolution using special SPECT collimators (Beekman and van der Have 2007b).

Resolution and image quality in coincidence PET are limited by (i) detector resolution and the effects of varying depth-of-interaction (DOI), (ii) non-collinearity of the annihilation gamma photons, (iii) random coincidences, (iv) coincidence losses and (v) the finite range of positrons. The first four factors are not prominent in pinhole SPECT: the negative consequences of detector blurring can be reduced to an acceptable level by choosing a sufficiently large pinhole magnification factor, while non-collinearity, random coincidences and coincidence loss do not play a role in collimated gamma ray imaging. These advantages of pinhole imaging may partly compensate for the limited sensitivity of SPECT; and, in a subset of imaging situations, the extension of MP-SPECT to the detection of high-energy annihilation photons may yield better resolution for positron emitters than contemporary small-animal PET (as will be shown below).

Simultaneous imaging of multiple tracers, each of which shows a different aspect of biological processes or pathology is attracting increasing interest. In SPECT, performing simultaneous dual-tracer imaging is often possible by setting multiple-energy windows (Kadrmas *et al* 1999, El Fakhri *et al* 2001, De Jong *et al* 2002, Meoli *et al* 2004, Zhou *et al* 2005, Du *et al* 2007, Neumann *et al* 2008, Steele *et al* 2008, Tai *et al* 2008, Terrovitis *et al* 2008, Yang *et al* 2008, Akutsu *et al* 2009). However, this is impractical in PET, where all gamma photons have equal energies. A system that allows the imaging of PET and SPECT tracers simultaneously makes it possible to visualize many new combinations of tracers in a single scan procedure, resulting in perfectly aligned images of a broad variety of different processes. Such a device can also be used to efficiently test how the properties of SPECT tracers are affected by their non-biological radioactive labels. Furthermore, combined PET/SPECT can reduce acquisition time for certain applications, and may be more cost-effective than using separate PET and SPECT devices.

Previously, positron emitters have been imaged in combination with Tc-99m using a single traditional pinhole. In (Tenney *et al* 2001) a uranium pinhole insert was used to image F-18 in a hot rod phantom in combination with Tc-99m; 3.9 mm rods could be resolved at best. Dual-isotope (Tc-99m-MIBI and FDG) SPECT on rats was investigated by Kubo *et al* (2004); a system resolution of 2.7 mm for FDG was attained. Clinical SPECT imaging of

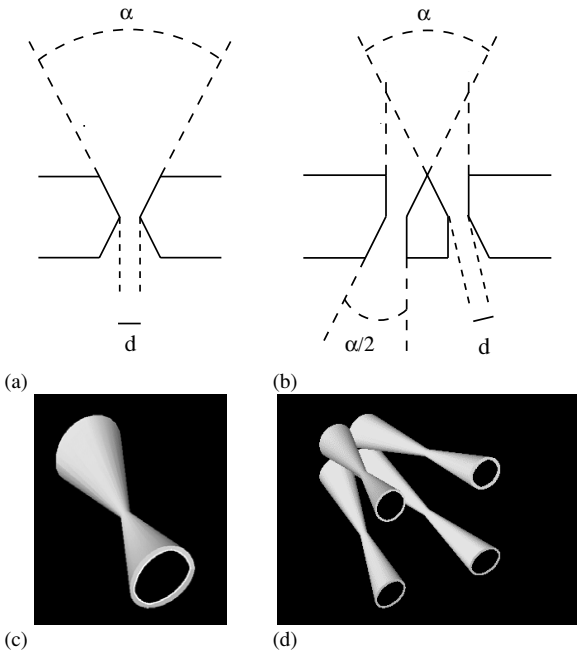

Figure 1. Concept of clustered pinholes: cross-sections through a traditional pinhole with opening angle α (a), and through a cluster of four pinholes, with opening angles of $\alpha/2$ each (b). Both geometries sample approximately the same FOV. Also shown are three-dimensional representations of a traditional pinhole (c) and a cluster of four pinholes (d).

positron emitters (FDG) with parallel hole collimators was demonstrated by Burt *et al* (1995) and Martin *et al* (1995) while simultaneous imaging of FDG with Tc-99m-labelled tracers was performed by Stoll *et al* (1994) and Sandler *et al* (1998). None of these approaches are suitable for high-resolution imaging of small experimental animals.

Severe pinhole edge penetration of 511 keV annihilation photons makes the multi-pinhole collimators currently used unsuitable for high-resolution imaging of positron emitters. Although reduction of the pinhole acceptance angles can, in principle, reduce the resolution loss due to edge penetration, such an improvement in resolution is at the cost of a reduced field-of-view (FOV) of each pinhole. The aim of this paper is to investigate the potential of clustered multi-pinhole SPECT (CMP, Beekman 2008), a novel pinhole geometry based on several pinholes with small acceptance angles grouped in clusters. In CMP, pinholes in a single cluster together sample the same FOV as a traditional pinhole with a larger opening angle (see figure 1). This newly proposed clustered multi-pinhole concept therefore has the potential to improve resolution without sacrificing FOV. In this paper, we compare CMP with more traditional multi-pinhole collimators.

2. Methods

CMP is compared to two geometries based on traditional pinholes. The traditional pinhole geometries we consider are (i) a currently used state-of-the-art SPECT collimator capable of imaging typical SPECT tracers with sub-half-mm resolutions and (ii) a collimator that has been specially adapted for imaging high-energy annihilation photons. Comparisons are performed

via ray trace simulations of a Jaszczak-like hot rod phantom, a tumour phantom and a mouse striatal brain phantom. Details of the geometries and simulations are given below.

2.1. Geometry of collimators and gamma-detectors

We assume that each of the collimator geometries we consider is placed at the centre of a U-SPECT-II system (MILabs, The Netherlands). This system has three stationary gamma detectors (active area of 51 $\times$ 38 cm, crystal thickness 9.5 mm) placed in a triangular configuration (van der Have *et al* 2009). The detectors have an intrinsic resolution of 3.5 mm and 12% of the 511 keV photons that fall onto the detector end up in the photo-peak window of 461–561 keV (Goorden and Beekman 2008). With an XYZ stage, an animal can be moved inside the collimator during imaging. This is used for imaging objects larger than the central-field-of-view (CFOV), the volume that is observed by all pinholes simultaneously. Using this dedicated acquisition protocol, entitled Scanning Focus Method (SFM; Vastenhouw and Beekman 2007a), the pinholes can collect gamma photons from different parts of the object. SFM leads to good images only when a dedicated reconstruction algorithm is used, rather than stitching together separate reconstructions of sub-volumes obtained from individual focus positions.

The three collimator geometries we compare are designed to have the same CFOV and the same collimator inner diameter (44 mm, large enough to allow for whole-body mouse imaging, Vastenhouw and Beekman 2007a). This design choice implies that the three geometries can image the same objects with an equal number of bed positions. The details of the geometries are provided below and illustrated in figure 2.

2.1.1. U-SPECT-II. The first geometry we consider is the general purpose U-SPECT-II mouse collimator with 0.6 mm pinholes (van der Have *et al* 2009). The geometry has 75 gold pinhole inserts, placed in five rings of 15 pinholes in a tungsten collimator. The pinhole centres are placed at a diameter of 48 mm, and the pinholes have an opening angle of $\alpha = 30^\circ$. The CFOV is cylindrical in shape with a diameter of 12.4 mm and a length of 12.9 mm. The U-SPECT-II system uses a shielding tube to prevent the projections of different pinholes from overlapping. Although we do not model the exact shape of the shielding tube in our simulations, its effect is partly included by assuming a collimator wall thickness that includes the wall thickness of the shielding tube. This is done such that the amount of simulated photons that penetrate the collimator wall directly matches that of U-SPECT-II. The thickness of collimator wall including shielding tube is 15 mm.

2.1.2. TMP. The next geometry we evaluate is also based on traditional pinholes, but it has been adapted to make it more suitable for imaging high-energy gamma-photons. Compared to U-SPECT-II, the wall of the tungsten collimator is thicker (45 mm), and the pinhole centres are placed at a larger diameter (56 mm). The purpose of these adaptations is to reduce photon penetration through the pinholes as well as directly through the collimator. To keep the CFOV equal to that of U-SPECT-II, the pinhole opening angles are set to $\alpha = 26^\circ$ (see figure 2(c)). Furthermore, since for 511 keV gamma photons the attenuation coefficient of tungsten (0.248 mm^{-1}) is almost equal to that of gold (0.286 mm^{-1}), we assume tungsten pinholes, instead of the gold inserts used in USPECT-II. The geometry has the same number of pinholes as U-SPECT-II and the same pinhole diameters (0.6 mm).

2.1.3. CMP. The clustered pinhole collimator design we consider resembles TMP, except that each traditional pinhole of TMP is replaced by a cluster of four pinholes, resulting in

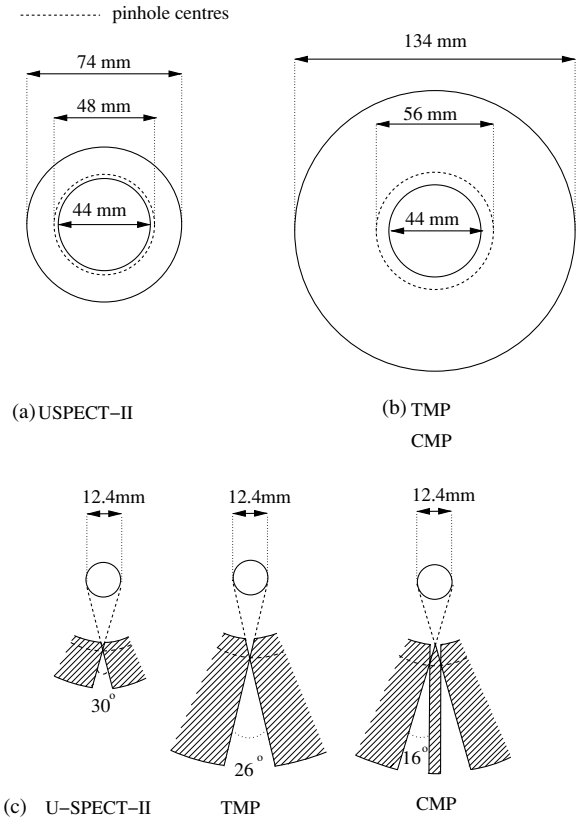

Figure 2. Collimator size and position of pinhole centres for (a) USPECT-II and (b) TMP and CMP. The pinholes in the three geometries are designed to have the same CFOV (c).

a design with 75 clusters or 300 pinholes. The CFOV is kept equal to that of TMP and U-SPECT-II by choosing an opening angle of $\alpha = 16^\circ$ for each individual pinhole in the cluster (see figure 2(c)). All other parameters are the same as those of TMP.

2.2. Digital phantom simulations

To evaluate the performance of CMP in different applications, we simulate three digital phantoms. The activity concentrations in the phantoms are set to values that occur in coincidence PET experiments. Details of the phantoms and activities are provided below.

2.2.1. Hot rod phantom. A Jaszczak-like hot rod phantom is used to visualize improvements in image resolution (figure 3(a)). It consists of six sectors with rods having sub-mm diameters of 0.6, 0.65, 0.7, 0.75, 0.8 and 0.9 mm. In this phantom, the distance between the centres of rods in a sector is twice the rod diameter. An activity concentration in the active areas of the hot rod phantom of 6.4 MBq ml^{-1} and a scan duration of 45 min are assumed (Tai *et al* 2003, 2005).

2.2.2. Mouse tumour phantom. The most common type of PET scan uses FDG to detect sites of high metabolic activity, which is frequently indicative of tumours. To assess performance

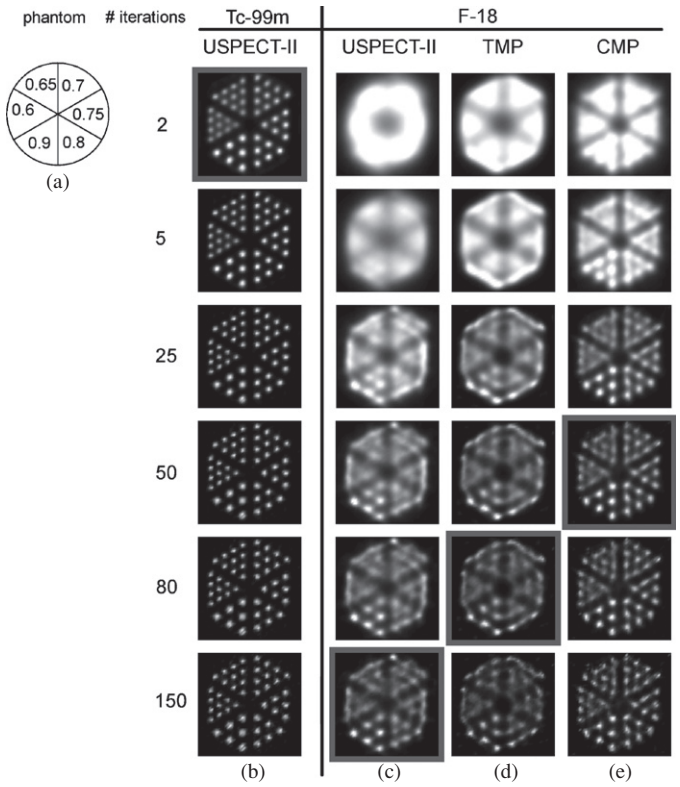

Figure 3. (a) Hot rod phantom with capillary diameters of 0.6, 0.65, 0.7, 0.75, 0.8 and 0.9 mm simulated for (b) Tc-99m with USPECT-II and for F-18 with (c) USPECT-II, (d) TMP and (e) CMP. Results are shown for different iteration numbers. Slice thickness is 1.5 mm. For each collimator the image with the lowest NMSE is indicated with a grey border.

of CMP for this important application, we simulate a phantom representing tumours implanted under the skin of a mouse in the hind left limb (xenografts, see figure 4(a)). The phantom consists of three tumours, with the largest one having a necrotic core. We assume that an activity of 20 MBq is injected and that the activity in the tumour is 5% of the injected dose per gram of tumour tissue (Wahl *et al* 1991). A scan duration of 45 min, starting 30 min post-injection, is assumed. Since FDG shows substantial uptake not only in tumours but also in the heart and brain, we include these organs in our simulation. For the mouse heart, we use the so-called MOBY phantom (Segars *et al* 2004); a mouse brain phantom was derived from (Franklin and Paxinos 2008; see also the next section). We assume that the activity concentration in the heart is five times higher than in the tumour, and that the concentration in the brain is 1.5 times as high (Wahl *et al* 1991). The activity concentration in other organs and in the blood is low and is assumed to be uniformly distributed over the mouse (which we approximate by an ellipsoid), with a background activity concentration 15 times smaller than that of the tumour.

2.2.3. Mouse striatal brain phantom. Several tracers, such as [18-F]FDOPA, [18-F]FMT and [18-F]FECNT, can be used to image aspects of the neurotransmitter system and study its relation to disorders such as Parkinson's disease (Honer *et al* 2006). In mouse models, this

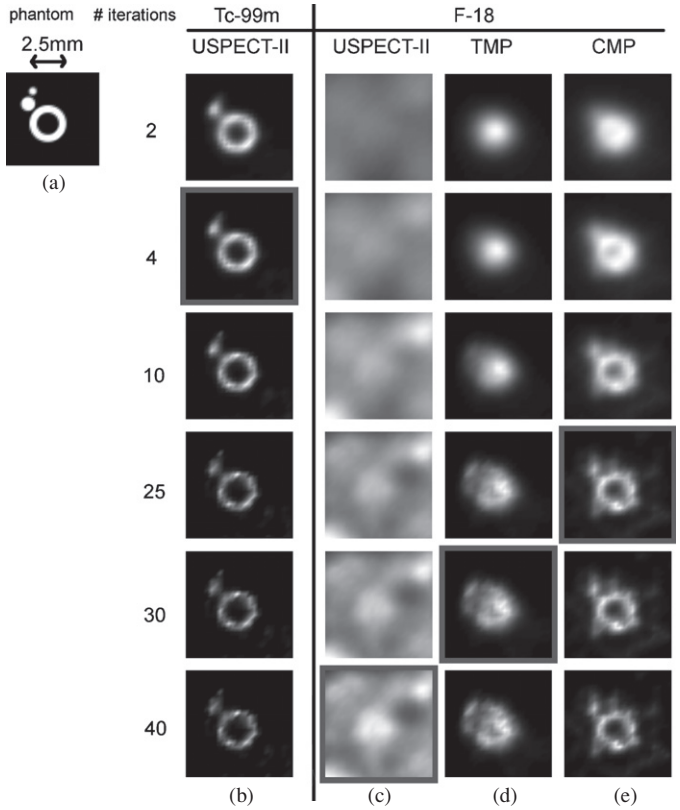

Figure 4. (a) A mouse tumour phantom simulated for (b) Tc-99m with USPECT-II and for F-18 with (c) USPECT-II, (d) TMP and (e) CMP. Results are shown for different iteration numbers. Slice thickness is 1 mm. For each collimator the image with the lowest NMSE is indicated with a grey border.

research is still limited by the resolution of available PET systems and the size of the target region (the mouse striatum is approximately 15 mm^3). To evaluate whether CMP can visualize the striatum and even sub-striatal structures, we have simulated a mouse striatal brain phantom, which we have derived from (Franklin and Paxinos 2008; see figure 5(a)). We assume that the activity concentration in striatum and olfactory tubercle is five times higher than in the surrounding brain tissue. Our simulations assume that an activity of 20 MBq is injected into the mouse (of which approximately 0.6% reaches the striatum) and that the mouse is scanned for 30 min, starting 1 min post-injection (Honer *et al* 2006). Since uptake in organs other than the striatum is low, we do not include other organs in our simulation but solely assume a background activity concentration that is ten times less than the activity in the striatum and that is distributed uniformly over the mouse (again approximated by an ellipsoid).

2.2.4. Simulator. Our simulator uses ray tracing to model the resolution-degrading effects of pinhole diameter and pinhole-edge penetration. The validity of this approximation was checked against Monte Carlo simulations (Goorden and Beekman 2008). Furthermore, positron range is taken into account, using a probability distribution for the annihilation point generated with Monte Carlo simulations. We have checked that the probability distribution

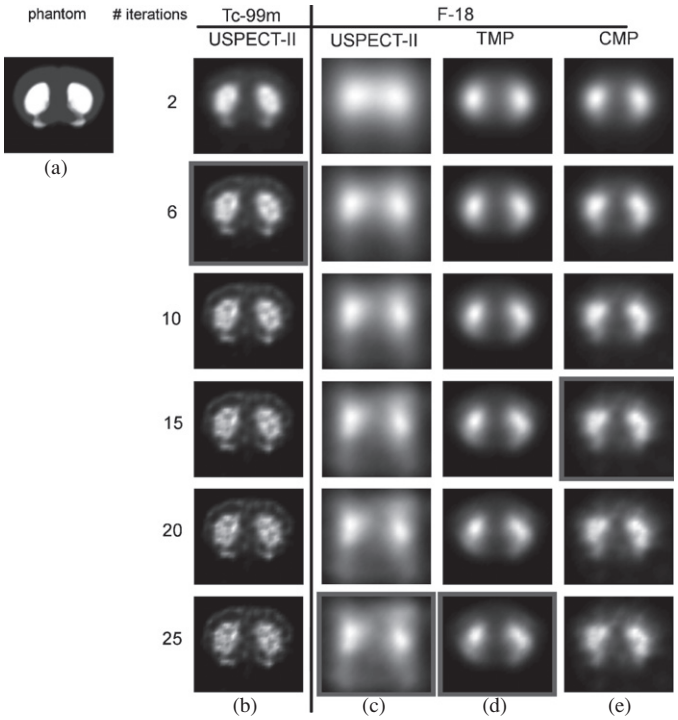

Figure 5. (a) A trans-axial slice through a mouse brain striatal phantom simulated for (b) Tc-99m with USPECT-II and for F-18 with (c) USPECT-II, (d) TMP and (e) CMP. Results are shown for different iteration numbers. Slice thickness is 0.5 mm. For each collimator the image with the lowest NMSE is indicated with a grey border.

matches with previous works (e.g. Levin and Hoffman 1999). In this paper we have modelled the detector by a Gaussian response with a FWHM of 3.5 mm. This value is based on experiments (Goorden and Beekman 2008). Poisson noise is added to the projection data. We simulate positron emitting tracers that are labelled with F-18. To provide a broader perspective, and to illustrate how our results for positron emitters compare to state-of-the-art high-resolution SPECT, we also show simulated images for Tc-99m for the U-SPECT-II collimator. For Tc-99m, we assume the same activity concentrations as for F-18, but we take into account that the capture efficiency of our detector is higher (90%, compared to 12%).

The voxel size of all phantoms is 0.125 mm, twice as small as the voxel size during image reconstruction. This is in order to emulate the fine resolution properties of real activity distributions. We assume five different bed positions (displaced by 1 mm only) for all phantoms to improve sampling.

2.3. Image reconstruction

A commonly used method of speeding up image reconstruction is ordered subset estimation maximization (OSEM, Hudson and Larkin 1994). Traditionally, each subset consists of a couple of projection views. For multi-pinhole SPECT, it was shown that pixel-based OSEM (POSEM), where pixels in each subset are spread out regularly over the projection views, leads to smaller deviations from maximum likelihood EM than traditional OSEM (Branderhorst *et al* 2010). In this paper, we have used POSEM with ten subsets for all reconstructions.

Relevant non-zero system-matrix elements were pre-calculated, using simulations of point sources. These simulations take into account the effect of detector blurring, finite pinhole diameter and pinhole-edge penetration, in the same manner as was done for the phantom simulations. Modelling positron range into the system matrix would result in a large increase in the number of non-zero matrix elements, and consequently a large increase in reconstruction time. Positron range is therefore accounted for by modelling it in the forward projection step of the reconstruction (Kamphuis *et al* 1998). The voxel size during reconstruction was 0.25 mm.

2.4. Evaluation of reconstructed images

In this paper, we have chosen to show a range of reconstructed images with different iteration numbers for each phantom. The image with the lowest normalized mean square error (NMSE) is always included in this range (for more than 10 iterations, we round off to a multiple of 5, while for more than 50 iterations we consider multiples of 10) and we indicate the location of the image with the lowest NMSE in our figures. Images are visually assessed by describing what details can be resolved with each particular collimation method.

2.5. Evaluation of sensitivities

We calculate the average sensitivity over the CFOV for each of the geometries considered in this paper. We do this by simulating a uniform activity distribution that has the size of the CFOV (a cylinder with a diameter of 12.4 mm and a length of 12.9 mm). These simulations use the same simulator that was used for the phantom simulations and that was described in section 2.2.

3. Results

In figure 3, we show simulated images for the hot rod phantom for a range of iteration numbers. Figure 3(b) shows images representing U-SPECT-II with Tc-99m. As shown in experimental studies (e.g. van der Have *et al* 2009), U-SPECT-II can reach sub-half-mm image resolution with Tc-99m. As a result, all rods are clearly separated in these images. However, when positron emitters are simulated with the same collimator (figure 3(c)), only the 0.9 mm rods are clearly resolved. Adapting the collimator by increasing the wall thickness (TMP) does improve the simulated images slightly, but rods smaller than 0.9 mm are still not clearly visible (figure 3(d)). The use of a cluster of pinholes instead of traditional pinholes leads to remarkable improvements in resolution: CMP is able to resolve rods with diameters of 0.7 mm and rods even smaller are partly visible.

In figure 4, we show simulated images of the mouse tumour phantom. With a Tc-99m labelled tracer, the necrotic core of the larger tumour and one of the smaller tumours can be distinguished, while the presence of a second smaller tumour is partly visible. If the same collimator (U-SPECT-II) is used for a tracer labelled with F-18, the tumour cannot be distinguished at all. This is due to the high levels of penetration directly through the collimator wall by photons coming from organs other than the tumour (in this case, mainly from the mouse heart and brain: see section 2.2.2, above). The presence of activity outside the CFOV is inevitable when imaging small animals. As a result, U-SPECT-II is unsuitable for small-animal studies with positron emitters: the wall needs to be thicker and longer pinholes are needed. Adapted in this way, a traditional multi-pinhole collimator can image the largest tumour (figure 4(d)), but it cannot detect the presence of the necrotic core nor can it clearly

resolve any of the smaller tumours. The use of CMP leads to remarkable improvements: CMP can resolve reduced activity in the necrotic core as well as the presence of a smaller tumour, although the two smaller tumours cannot be resolved separately.

Figure 5 shows images of the mouse striatal brain phantom. Previous experimental studies had shown that U-SPECT-II can visualize sub-striatal structures, such as the olfactory tubercle (Vastenhouw *et al* 2007b), something that is also apparent from our simulated images (figure 5(b)). As for the tumour phantom, direct penetration of 511 keV gamma photons through the collimator wall makes U-SPECT-II unsuitable for imaging positron emitters (figure 5(c)). Collimators with increased wall thickness, however, can provide much more detail (figures 5(d) and (e)): the olfactory tubercle cannot be resolved as clearly as with Tc-99m, but some sub-striatal shapes remain visible. CMP does show more detail than TMP, but the difference is not as striking as for the other phantoms.

The simulated average sensitivity of U-SPECT-II with Tc-99m was found to be 0.18%, which perfectly agrees with experimental values (van der Have *et al* 2009). When F-18 is used in U-SPECT-II the sensitivity increase due to stronger pinhole edge penetration is partly compensated by the decreased detector sensitivity at 511 keV; in total we found a sensitivity of 0.53%. For TMP and CMP with F-18 we found sensitivities of 0.19% and 0.25%, respectively.

4. Discussion

Image resolutions of the different collimator geometries were assessed using iterative reconstruction of hot rods (see figure 3(c)). From these simulated images it might appear that a SPECT collimator optimized for high-resolution imaging of typical SPECT tracers can reach image resolutions of about 0.9 mm when imaging positron emitters. However, when small animals are imaged, where activity is also present in organs outside the CFOV of the collimator, the severe penetration of the collimator wall will have a large adverse effect on the quality of reconstructed images (as is apparent in figures 4(c) and 5(c)). This makes it necessary to use a specially adapted collimator with a thicker wall and longer pinholes than is typical in SPECT collimators. Although these adaptations are necessary for imaging small animals, the increased wall thickness and the use of longer pinholes alone do not significantly improve the simulated images of the hot rod phantom (figure 3(d)). The use of clustered pinholes with smaller acceptance angles than traditional pinholes, however, has a large impact on image resolution: hot rods as small as 0.7 mm are resolved (figure 3(e)), a resolution that is significantly better than what is obtainable with state-of-the art PET devices. Such a high resolution can, for example, be useful when tracer distributions in tumours need to be assessed (see figure 4). CMP can provide much more information about tumour characteristics than TMP (e.g. whether a radio-labelled molecule accumulates in a necrotic core or only in the living cancer shells outside the tumour, or whether metastases are present). For imaging of sub-striatal structures, such as those shown in figure 5, the clustered pinhole geometry provides more detail than TMP, although the improvement of CMP over this traditional pinhole geometry is less pronounced for this specific example than for the other studies in this paper. We believe that this is due to the very low tracer concentration that is present when imaging the striatum (less than 1% of the injected activity reaches the striatum).

Although the reconstructed resolution of CMP is a distinct improvement over high-end small-animal coincidence PET, the sensitivity of our newly proposed device cannot reach the level achieved by coincidence PET devices. We would like to stress, however, that sensitivity in itself does not determine image quality; it is the combination of sensitivity and the information content per detected photon that determines how much image detail can be obtained. We believe that for applications where only small parts of a mouse are imaged and sufficient

activity can be used (such as in the tumours shown in figure 4), the limited sensitivity does not necessarily pose a great problem. Rather, our simulations indicate that structures that cannot be resolved by any traditional PET device can be visualized with clustered pinholes. In whole-body imaging, the focus needs to move more, resulting in decreased sensitivity. Although it has been shown that MP-SPECT with SPECT tracers is able to achieve sub-mm image resolutions in whole-body imaging (Vastenhouw and Beekman 2007a), further investigations are needed to find out if this also holds for CMP.

In principle, alternative ways of reducing edge penetration exist besides the clustered pinhole geometry proposed in this paper. One is the use of a collimator with traditional pinholes, each of which has a small opening angle. However, such a design has a strongly reduced CFOV compared to typical SPECT collimators and consequently sampling the volume-of-interest requires an undesirably large number of steps: a reduction of the opening angle by a factor of 2 already results in an eightfold increase in the number of steps. The clustered pinhole geometry presented here does not have this disadvantage: it is able to attain higher image resolutions than traditional multi-pinhole collimators with the same CFOV.

In this paper we have used ray tracing to simulate the passage of 511 keV gamma photons through the collimator. This means that we have neglected photons that undergo a Compton scattering event. In (Goorden and Beekman 2008) we have used full Monte Carlo simulations to determine the density of scattered photons on the detector. We find that this density is an order of magnitude lower than the density of photons that come from the background activity in the tumour phantom and brain phantom used in this paper. We therefore believe that neglecting scattered photons does not significantly influence the results.

5. Conclusion

We have shown that pinhole geometries based on a cluster of pinholes are very promising for the purpose of imaging positron emitting tracers and possibly the combined imaging of positron emitting and SPECT tracers. Our simulations indicate that the resolution that can be obtained with clustered pinholes surpasses that of state-of-the-art small-animal PET devices when imaging objects with the size of mouse organs. The high image resolution, the possibility of performing simultaneous dual-tracer imaging, and the cost savings enabled by the fact that only a single scanner is needed for PET and SPECT may open unique research opportunities.

References

Akutsu Y, Kaneko K, Kodama Y, Li H L, Nishimura H, Hamazaki Y, Suyama J, Shinozuka A, Gokan T and Kobayashi Y 2009 Technetium-99m pyrophosphate/thallium-201 dual-isotope SPECT imaging predicts reperfusion injury in patients with acute myocardial infarction after reperfusion *Eur. J. Nucl. Med. Mol. Imaging.* **36** 230–6

Andringa G, Drukarch B, Bol J G J M, de Bruin K, Sorman K, Habraken J B A and Booij J 2005 Pinhole SPECT imaging of dopamine transporters correlates with dopamine transporter immunohistochemical analysis in the MPTP mouse model of Parkinson's disease *Neuroimage* **26** 1150–8

Beekman F J 2008 Collimator with pinhole clusters *European Patent Application* no 07076118.4

Beekman F J and van der Have F 2007a The pinhole: gateway to ultra-high-resolution three-dimensional radionuclide imaging *Eur. J. Nucl. Med. Mol. Imaging.* **34** 151–61

Beekman F J and van der Have F 2007b High resolution tomography of positron emitters using highly focused pinhole collimation *J. Nucl. Med. Meeting Abstracts* **48** 92P-b

Beekman F J, van der Have F, Vastenhouw B, van der Linden A J A, van Rijk P P, Burbach J P H and Smidt M P 2005 U-SPECT-I: a novel system for submillimeter-resolution tomography with radiolabeled molecules in mice *J. Nucl. Med.* **46** 1194–200

Blanckaert P, Burvenich I, Staelens S, de Bruyne S, Moerman L, Wyffels L and de Vos F 2009 Effect of cyclosporin A administration on the biodistribution and multipinhole mu SPECT imaging of [I-123]R91150 in rodent brain *Eur. J. Nucl. Med. Mol. Imaging* **36** 446–53

Branderhorst W, Vastenhouw B and Beekman F J 2010 Pixel-based subsets for rapid multi-pinhole SPECT reconstruction *Phys. Med. Biol.* submitted

Burt R W, Perkins O W, Oppenheim B E, Schauwecker D S, Stein L, Wellman H N and Witt R M 1995 Direct comparison of Fluorine-18-FDG SPECT, Fluorine-18-FDG PET and rest TL-201 SPECT for detection of myocardial viability *J. Nucl. Med.* **36** 176–9

Davis S L, Be N A, Lamichhane G, Nimmagadda S, Pomper M G, Bishai W R and Jain S K 2009 Bacterial thymidine kinase as a non-invasive imaging reporter for Mycobacterium tuberculosis in live animals *PloS One* **4** e6297

De Jong H W A M, Beekman F J, Viergever M A and van Rijk P P 2002 Simultaneous Tc-99m/Tl-201 dual-isotope SPET with Monte Carlo-based down-scatter correction *Eur. J. Nucl. Med. Mol. Imaging* **29** 1063–71

Deroose C M, Reumers V, Debyser Z and Baekelandt V 2009 Seeing genes at work in the living brain with non-invasive molecular imaging *Curr. Gene Ther.* **9** 212–38

Du Y, Tsui B M W and Frey E C 2007 Model-based crosstalk compensation for simultaneous Tc-99m/I-123 dual-isotope brain SPECT imaging *Med. Phys.* **34** 3530–43

El Fakhri G, Moore S C, Maksud P, Aurengo A and Kijewski M F 2001 Absolute activity quantitation in simultaneous I-123/Tc-99m brain SPECT *J. Nucl. Med.* **42** 300–8

Franklin K B J and Paxinos G 2008 *The Mouse Brain in Stereotaxic Coordinates* (Amsterdam: Elsevier)

Funk T, Després P, Barber W C, Shah K S and Hasegawa B H 2006 A multipinhole small animal SPECT system with submillimeter spatial resolution *Med. Phys.* **33** 1259–67

Furenlid L R, Wilson D W, Chen Y C, Kim H, Pietraski P J, Crawford M J and Barrett H H 2004 FastSPECT II: a second-generation high-resolution dynamic SPECT imager *IEEE Trans. Nucl. Sci.* **51** 631–5

Goorden M C and Beekman F J 2008 A Monte Carlo study of scattering and attenuation of 511 KeV gamma rays in a pinhole *IEEE NSS/MIC Meeting Abstracts* M10-272

Hesterman J Y, Kupinski M A, Furenlid L R, Wilson D W and Barrett H H 2007 The multi-module, multi-resolution system ((MR)-R-3): a novel small-animal SPECT system *Med. Phys.* **34** 987–93

Honer M, Hengerer B, Blagoev M, Hintermann S, Waldmeier P, Schubiger P A and Ametamey S M 2006 Comparison of [18F]FDOPA, [18F]FMT and [18F]FECNT for imaging dopaminergic neurotransmission in mice *Nucl. Med. Biol.* **33** 607–14

Hudson H M and Larkin R S 1994 Accelerated image-reconstruction using ordered subsets of projection data *IEEE Trans. Med. Imaging* **13** 601–9

Ishizu K, Mukai T, Yonekura Y, Pagani M, Fujita T, Magata Y, Nishizawa S, Tamaki N, Shibasaki H and Konishi J 1995 Ultra-high resolution SPECT system using four pinhole collimators for small animal studies *J. Nucl. Med.* **36** 2282–7

Jaszczak R J, Li J Y, Wang H L, Zalutsky M R and Coleman R E 1994 Pinhole collimation for ultra-high-resolution, small-field-of-view SPECT *Phys. Med. Biol.* **39** 425–37

Kadrmas D J, Frey E C and Tsui B M W 1999 Simultaneous technetium-99m/thallium-201 SPECT imaging with model-based compensation for cross-contaminating effects *Phys. Med. Biol.* **44** 1843–60

Kamphuis C, Beekman F J, van Rijk P P and Viergever M A 1998 Dual matrix ordered subsets reconstruction for accelerated 3D scatter compensation in single-photon emission tomography *Eur. J. Nucl. Med.* **25** 8–18

Kubo N, Zhao S J, Kinda A, Motomura N, Katoh C, Kuge Y and Tamaki N 2004 An ultra-high-energy collimator for small animal imaging in dual-isotope study of F-18 and Tc-99m *Int. Congr. Ser.* **1264** 275–9

Levin C S and Hoffman E J 1999 Calculation of positron range and its effect on the fundamental limit of positron emission tomography system spatial resolution *Phys. Med. Biol.* **44** 781–99

Liu Z, Kastis G A, Stevenson G D, Barrett H H, Furenlid L R, Kupinski M A, Patton D D and Wilson D W 2002 Quantitative analysis of acute myocardial infarct in rat hearts with ischemia-reperfusion using a high-resolution stationary SPECT system *J. Nucl. Med.* **43** 933–39

Martin W H, Delbeke D, Patton J A, Hendrix B, Weinfeld Z, Ohana I, Kessler R M and Sandler M P 1995 FDG-SPECT— correlation with FDG PET *J. Nucl. Med.* **36** 988–95

McElroy D P, MacDonald L R, Beekman F J, Wang Y C, Patt B E, Iwanczyk J S, Tsui B M W and Hoffman E J 2002 Performance evaluation of A-SPECT: a high resolution desktop pinhole SPECT System for imaging small animals *IEEE Trans. Nucl. Sci.* **49** 2139–47

Meoli D F *et al* 2004 Noninvasive imaging of myocardial angiogenesis following experimental myocardial infarction *J. Clin. Invest.* **113** 1684–91

Metzler S D, Jaszczak R J, Patil N H, Vemulapalli S, Akabani G and Chin B B 2005 Molecular imaging of small animals with a triple-head SPECT system using pinhole collimation *IEEE Trans. Med. Imaging* **24** 853–62

Neumann D R, Obuchowski N A and DiFilippo F P 2008 Preoperative I-123/(99)mTc-sestamibi subtraction SPECT and SPECT/CT in primary hyperparathyroidism *J. Nucl. Med.* **49** 2012–17

Nikolaus S, Antke C, Kley K, Beu M, Wirrwar A and Müller H W 2009 Pretreatment with haloperidol reduces (123)I-FP-CIT binding to the dopamine transporter in the rat striatum: an *in vivo* imaging study with a dedicated small-animal SPECT camera *J. Nucl. Med.* **50** 1147–52

Sandler M P, Bax J J, Patton J A, Visser F C, Martin W H and Wijns W 1998 Fluorine-18-fluorodeoxyglucose cardiac imaging using a modified scintillation camera *J. Nucl. Med.* **39** 2035–43

Schramm N U, Ebel G, Engeland U, Schurrat T, Béhé M and Behr T M 2003 High-resolution SPECT using multipinhole collimation *IEEE Trans. Nucl. Sci.* **50** 315–20

Segars W P, Tsui B M W, Frey E C, Johnson G A and Berr S S 2004 Development of a 4-D digital mouse phantom for molecular imaging research *Mol. Imaging Biol.* **6** 149–59

Steele P P, Kirch D L and Koss J E 2008 Comparison of simultaneous dual-isotope multipinhole SPECT with rotational SPECT in a group of patients with coronary artery disease *J. Nucl. Med.* **49** 1080–9

Stoll H P, Hellwig N, Alexander C, Ozbek C, Schieffer H and Oberhausen E 1994 Myocardial metabolic imaging by means of fluorine-18 deoxyglucose/technetium-99m sestamibi dual-isotope single-photon emission tomography *Eur. J. Nucl. Med.* **21** 1085–93

Strand S E, Ivanovic M, Erlandsson K, Franceschi D, Button T, Sjogren K and Weber D D 1994 Small animal imaging with pinhole single photon emission computed-tomography *Cancer* **73** 981–4

Tai J H, Nguyen B, Wells R G, Kovacs M S, McGirr R, Prato F S, Morgan T G and Dhanvantari S 2008 Imaging of gene expression in live pancreatic islet cell lines using dual-isotope SPECT *J. Nucl. Med.* **49** 94–102

Tai Y C, Chatziioannou A F, Yang Y F, Silverman R W, Meadors K, Siegel S, Newport D F, Stickel J R and Cherry S R 2003 MicroPET II: design, development and initial performance of an improved microPET scanner for small-animal imaging *Phys. Med. Biol.* **48** 1519–37

Tai Y C, Ruangma A, Rowland D, Siegel S, Newport D F, Chow P L and Laforest R 2005 Performance evaluation of the microPET focus: a third-generation microPET scanner dedicated to animal imaging *J. Nucl. Med.* **46** 455–63

Tenney C R, Tornai M P, Smith M F, Turkington T G and Jaszczak R J 2001 Uranium pinhole collimators for 511-keV photon SPECT imaging of small volumes *IEEE Trans. Nucl. Sci.* **48** 1483–89

Terrovitis J *et al* 2008 Ectopic expression of the sodium-iodide symporter enables imaging of transplanted cardiac stem cells *in vivo* by single-photon emission computed tomography or positron emission tomography *J. Am. Coll. Cardiol.* **52** 1652–60

van der Have F, Vastenhouw B, Ramakers R M, Branderhorst W, Krah J O, Ji C, Staelens S G and Beekman F J 2009 U-SPECT-II: an ultra-high-resolution device for molecular small-animal imaging *J. Nucl. Med.* **50** 599–605

Vastenhouw B and Beekman F J 2007a Submillimeter total-body murine imaging with U-SPECT-I *J. Nucl. Med.* **48** 487–93

Vastenhouw B, van der Have F, van der Linden A J A, von Oerthel L, Booij J, Burbach J P H, Smidt M P and Beekman F J 2007b Movies of dopamine transporter occupancy with ultra-high resolution focusing pinhole SPECT *Mol. Psychol.* **12** 984–7

Wahl R L, Hutchins G D, Buchsbaum D J, Liebert M, Grossman H B and Fisher S 1991 18F-2-deoxy-2-fluoro-d-glucose uptake into human xenografts *Cancer* **67** 1544–50

Walrand S, Jamar F, de Jong M and Pauwels S 2005 Evaluation of novel whole-body high-resolution rodent SPECT (Linoview) based on direct acquisition of linogram projections *J. Nucl. Med.* **46** 1872–80

Wild D, Behe M, Wicki A, Storch D, Waser B, Gotthardt M, Keil B, Christofori G, Reubi J C and Macke H R 2006 [Lys(40) (Ahx-DTPA-In-111)NH2]exendin-4, a very promising ligand for glucagon-like peptide-1 (GLP-1) receptor targeting *J. Nucl. Med.* **47** 2025–33

Yang Y K, Yeh T L, Yao W J, Lee I H, Chen P S, Chiu N T and Lu R B 2008 Greater availability of dopamine transporters in patients with major depression— a dual-isotope SPECT study *Psychiatry Res. Neuroimaging* **162** 230–5

Zhou R, Thomas D H, Qiao H, Bal H S, Choi S R, Alavi A, Ferrari V A, Kung H F and Acton P D 2005 *In vivo* detection of stem cells grafted in infarcted rat myocardium *J. Nucl. Med.* **46** 816–22